Supporting Information

Single-Atom Nickel Terminating sp^2 and sp^3 Nitride in Polymeric Carbon Nitride for Visible-Light Photocatalytic Overall Water Splitting

Yanrui Li, Yiqing Wang, Chung-Li Dong, Yu-Cheng Huang, Jie Chen, Zhen Zhang, Fanqi Meng, Qinghua Zhang, Yiliang Huangfu, Daming Zhao, Lin Gu, Shaohua Shen*

Experimental Section

Supplementary Figures and Tables

Figure S1. Charge carrier migration in PCN.

Figure S2. Reaction pathway for the synthesis of PCN.

Figure S3. TEM images of PCN and PCNNi.

Figure S4. The low-magnification EDX mapping of PCNNi.

Figure S5. Thermogravimetric analysis of PCN and PCNNi .

Figure S6. Nitrogen adsorption-desorption isotherms of PCN and PCNNi.

Figure S7. Ni 2p and C 1s XPS analysis of PCN and PCNNi.

Figure S8. Solid-state ^{13}C CP-MAS NMR spectra of PCN and PCNNi.

Figure S9. Ni 2p XPS spectra of PCNNi-T.

Figure S10. N 1s XPS spectra of PCN-T and PCNNi-T.

Figure S11. XPS valence band spectra of PCN and PCNNi.

Figure S12. The apparent quantum yields of PCNNi-3 for H$_2$ evolution

Figure S13. The raw GC spectrum detected by the thermal conductivity detector (TCD).

Figure S14. Photocatalytic stability for overall water splitting, and EXAFS and XANES spectra for PCNNi before and after photocatalytic reaction.

Figure S15. The steady-state PL spectra of PCN and PCNNi.

Figure S16. Electrochemical impedance spectra of PCN and PCNNi.

Figure S17. Differential charge density mapping of the M-L unit.

Figure S18. Theoretically calculated for reaction pathways and proposed mechanisms of photocatalytic pure water splitting for PCNNi with single-atom Ni coordinated with sp^3 N_B.

Table S1. Summary of Ni contents of PCNNi in different synthesis batches.

Table S2. FWHM of PCN and PCNNi.

Table S3. Elemental analysis results of PCN and PCNNi.

Table S4. Summary of N 1s core-level binding energies of PCN and PCNNi.

Experimental Section

Materials

Melamine ($C_3H_6N_6$, ≥99.0%), Nickel chloride hexahydrate ($NiCl_2·6H_2O$, ≥98.5%), ethanol (C_2H_6O, ≥99.7%) were purchased from Sinopharm Chemical Reagent Co., Ltd. All the materials were of analytical grade and used as received without further purification. Ultrahigh purity argon (Ar, ≥99.999%) was provided by Shaanxi Xinkang Medical Oxygen Co., Ltd. Deionized water, with a resistivity of 18.25 MΩ·cm, was used throughout the experiments.

Preparation of pure PCN

PCN was synthesized by a traditional thermal polymerization strategy as previously reported [1]. In detail, melamine was heated at 550 °C for 4 h in Ar atmosphere with a ramping rate of 2 °C/min. The obtained yellow agglomerates were smashed into powder.

Preparation of PCNNi

PCNNi was synthesized via thermal polymerization similar to PCN, with desired amounts of $NiCl_2·6H_2O$ added in melamine. Specifically, melamine (100 mg) and $NiCl_2·6H_2O$ (0.6 mg, 1.23 mg, 2.5 mg, 4.9 mg) were mixed and triturated in agate mortar for 30 min, and then heated at 550 °C for 4 h in Ar atmosphere with a ramping rate of 2 °C/min. The samples were obtained after naturally cooled down to room temperature under argon gas flow, followed by washing with deionized H_2O and ethanol, and then dried at 60 °C overnight. The inductively coupled plasma (ICP) test results confirm the Ni contents to be 0.3 wt%, 0.5 wt%, 1.0 wt%, and 1.9 wt%. Then, these PCNNi with different Ni contents were denoted as PCNNi-1, PCNNi-2, PCNNi-3, and PCNNi-4, respectively.

Preparation of PCN-T and PCNNi-T (T = 390, 420, 500) intermediate products

Thermal polymerization intermediate products, PCN-T and PCNNi-T (T = 390, 420, 500), were obtained at different temperatures (390 °C, 420 °C, 500 °C) during the polymerization reactions for the synthesis of PCN and PCNNi, respectively. The reactions were terminated at different temperatures, with samples naturally cooled down to room temperature under argon gas flow.

Characterizations

Transmission electron microscopy (TEM) images were recorded at FEI Tecnai G2 F30 S-Twin transmission electron microscope at an accelerating voltage of 300 kV. High-angle annular dark-field (HAADF) image in scanning transmission electron microscopy (STEM) mode was carried out on JEOL ARM200 transmission electron microscope operating at 200 KeV (JEOL, Tokyo, Japan). X-ray diffraction (XRD) patterns were collected on a PANalytical X'pert MPD Pro diffractometer operated at 40 kV and 40 mA using Ni-filtered Cu Kα irradiation (Wavelength = 1.5406 Å). Fourier transform infrared (FTIR) spectra were recorded on a Bruker Vextex 70 FTIR spectrometer using the KBr pellet technique. The synchrotron X-ray spectroscopic (XAS) measurements at Ni, C and N K-edge were performed at BL20A, at National Synchrotron Radiation Research Center, Taiwan. X-ray photoelectron spectroscopy (XPS) data were obtained on a Kratos Axis Ultra DLD instrument with a monochromatized Al Ka line source (150 W). All the binding energies were referenced to the C 1 s peak at 284.8 eV. The steady-state photoluminescence (PL) emission spectra and time-resolved transient PL decay spectra were carried out at room temperature using a PTI QM-4 fluorescence spectrophotometer. UV–vis diffuse reflectance spectra were recorded on a Cary Series UV–vis-NIR spectrophotometer (Agilent Technologies). The Ni contents in PCNNi were determined by using inductively coupled plasma mass spectroscopy (ICP-MS) on the Perkin Elmer Optima 8300 ICP-OES instrument. The solid-state ^{13}C NMR spectra were acquired on 400 MHz solid-state NMR spectrometer (AVANCE HD, Bruker, Germany). Elemental analysis was performed on an elemental analyzer (Elemental Analysensysteme GmnH, Germany).

The nitrogen adsorption–desorption isotherms were collected at 77 K using surface area and porosity analyzer (Micromeritics ASAP2020KMP + Vapor).

Determination of electron transfer number

The electron transfer number was determined by using rotating disk-ring electrodes (RRDE) testing system [2]. RRDE experiments were carried out in N_2 saturated ultrapure water with a scan rate of 10 mV·s^{-1} and a rotating speed of 1600 rpm. The ring potential was kept at 0.9 V vs. Saturated calomel electrode (SCE) and the disk potential was set at open circuit potential. A Chi 920C electrochemical workstation was applied to record the process and data. The electron transfer number (n) could be calculated according to the following formula:

$$n = \frac{4I_d}{I_d + I_r/N}$$

Where I_d and I_r represent the disk and ring current, respectively. The N is the rotating disk ring electrode (RRDE) collection efficiency determined to be 0.43.

Electrochemical impedance spectroscopy (EIS) measurement

Electrochemical impedance spectroscopy (EIS) measurements were performed on a Chi 920C electrochemical workstation with a standard three-electrode system with the frequency range from 0.1 to 10^5 Hz at 1.45 V versus the Ag/AgCl electrode. 0.05 M Na_2SO_4 aqueous solution was used as the electrolyte.

Photocatalytic tests for pure water splitting into H_2 and H_2O_2

Photocatalytic water splitting reactions were performed in a 100-mL gas-closed Pyrex reactor. In a typical photocatalytic reaction, 30 mg of photocatalysts were dispersed in 80 mL of deionized water. Nitrogen was purged through the on-line reactor for 20 min before reaction to remove the residual air. A 300 W Xe lamp with a 420 nm cutoff filter was used to trigger the photocatalytic overall water splitting. The temperature of the reaction solution was kept at 35 °C via a circulating water pump during the experiment. The reaction products were determined by an online gas chromatograph. The concentration of H_2O_2 was determined by UV-vis spectroscopy with *o*-tolidine as the peroxide indicator. 2.0 mL of reaction suspension was taken immediately after the irradiation and 0.5 mL of 1% *o*-tolidine in 0.1 M HCl was added to the suspension, waiting for 2 min. Next, 2 mL of 1 M HCl was introduced into above mixture for acidification. Finally, the suspension was centrifuged (10000 rpm) to remove the catalyst and recorded on a Cary Series UV–vis-NIR spectrophotometer (Agilent Technologies). The apparent quantum yield (AQY) for H_2 evolution was measured under the same photocatalytic reaction condition with bandpass filters of 380 nm, 420 nm and 500 nm used to provide the monochromic light. The number of incident photons was determined by an irradiation meter (AvaSpec-2048). The AQY value was calculated according to the following Equation (1):

$$AQY(\%) = \frac{nunmber\ of\ reacted\ electrons}{nunmber\ of\ incident\ photons} \times 100\% \tag{1}$$

$$= \frac{nunmber\ of\ evolved\ hydrogen\ molecules \times 2}{nunmber\ of\ incident\ photons} \times 100\%$$

Theoretical Calculations

First-principles density functional theory (DFT) calculations were performed using the Vienna ab initio simulation package (VASP) [3-5] and the projector augmented wave (PAW) method [6]. The exchange-correlation effects were treated in generalized gradient approximation (GGA) with the Perdew-Burke-Ernzerhof (PBE) potential [7]. The kinetic energy cutoff was chosen to be 520 eV. Brillouin zone integration was sampled with 3×3×1 and 3×3×1 Monkhorst-Pack mesh K-points for bulk and surface calculation. The optimized structural parameters for PCN and PCNNi are a = 16.8936 Å, b = 12.7690Å, c =3.2700Å. The PCN (001) and PCNNi (001) surface was modeled by a periodic three three-layers with an exposed surface area of 16.8936×12.7690 $Å^2$. The slabs were set by a vacuum region of 15 Å. The adsorbates and the top layers of the surfaces are allowed to be fully relaxed and optimized until convergence to 10^{-5} eV in total energy and 0.01 eV/Å in the forces, while the bottom two three-layers of PCN (001) and PCNNi (001) were kept fixed at the calculated bulk positions. Based on the charge density calculation, the bader charge distribution of each atom was determined using the bader charge calculation method proposed by Henkelman's group [8-10]. The obtained transition states were further confirmed to possess only one single imaginary frequency. The energy of proton-electron pairs ($H^+ + e^-$) was treated as $E(H^+ + e^-) = \frac{1}{2}E(H_2)$.

Supplementary Figures and Tables

The photoexcited electrons and holes generated in the heptazine units are demonstrated to undergo five possible migration pathways (Figure S1): (1) interplanar migration along the π-stacking direction, (2) fast recombination of electron-hole pairs confined in the heptazine units, (3) transport from one s-heptazine unit to another with different symmetric planes in the same heptazine-based polymer chains, (4) transport between adjacent heptazine-based polymer chains, which will be always interrupted by hydrogen bonds, resulting in the recombination of electrons and holes, (5) intrachain migration along the polymer chains through bridging N atoms, which encounter charge recombination during the migration. Thus, the charge recombination in aromatic conjugate ring and during the intrachain migration as well as the interrupted charge transfer by the hydrogen bonds would be the limits for the charge carrier separation and transfer in PCN [11].
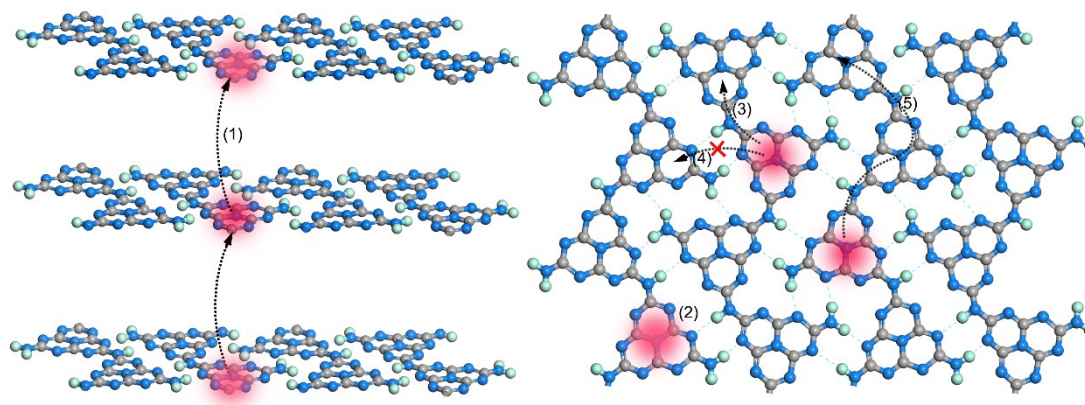
Figure S1. Charge carrier migration in (a) the π-stacking direction and (b) the intraplanar migration. The blue, gray and green spheres are the N, C and H atoms, respectively.

The thermal polymerization reaction is a combination of polyaddition and polycondensation processes [12]. As shown in Figure S2, the nitrogen-rich precursor of melamine is condensed to melam at 335 °C, then the heptazine units are formed over 390 °C. By heating to 425 °C, melem are produced, hydrogen bonding formed between heptazine units with the groups of NH_2 [13]. Then, the polymer chains, a linear polymer of interconnected heptazine, forms at 500 °C. Finally, PCN is obtained at 550 °C.
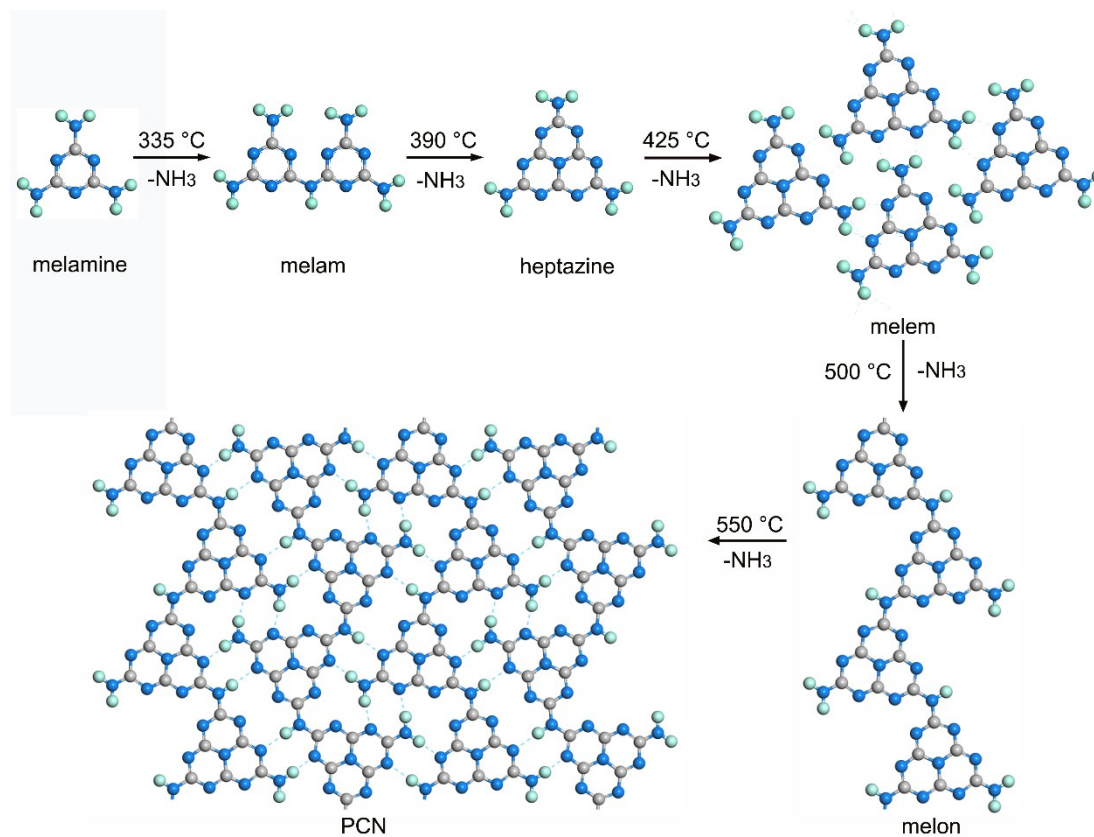

Figure S2. Reaction pathway of the thermal polymerization of melamine to for the synthesis of PCN. The blue, gray and green spheres are the N, C and H atoms, respectively.
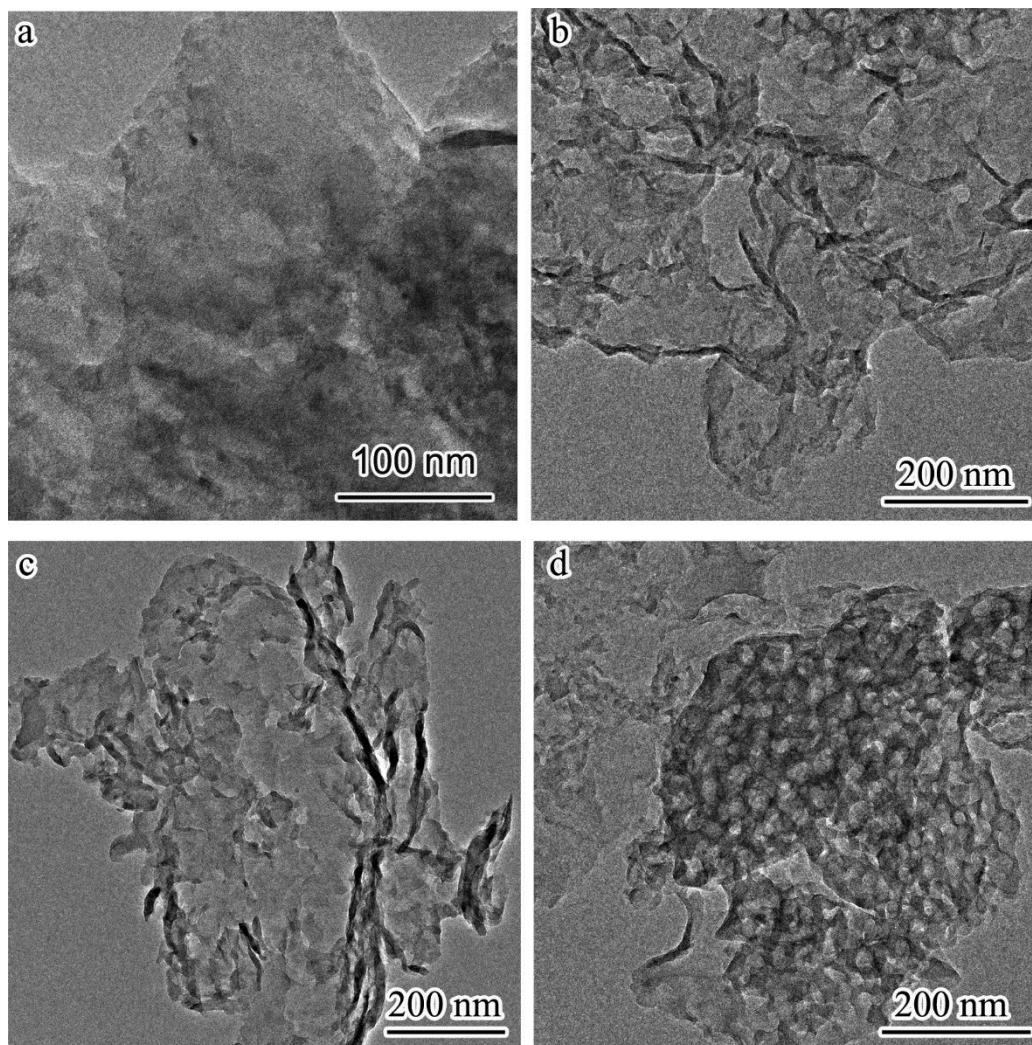
Figure S3. TEM images of a) PCN, b) PCNNi-1, c) PCNNi-2, d) PCNNi-4.

As shown in the low-magnification EDX mapping of PCNNi-4 with the maximum content of Ni (Figure S4), Ni species are not likely to aggregate into particles, but are well dispersed in PCNNi.
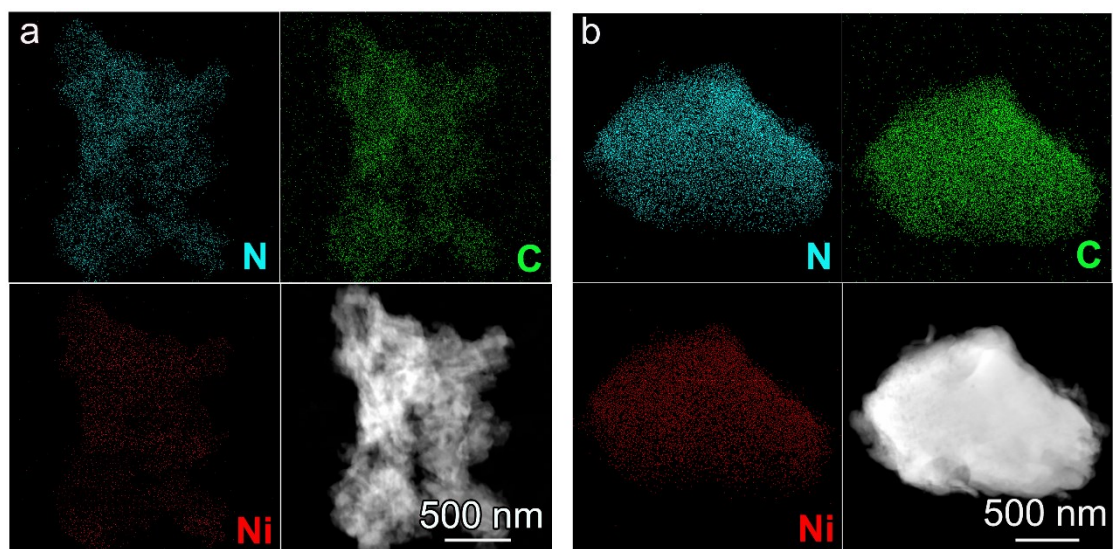
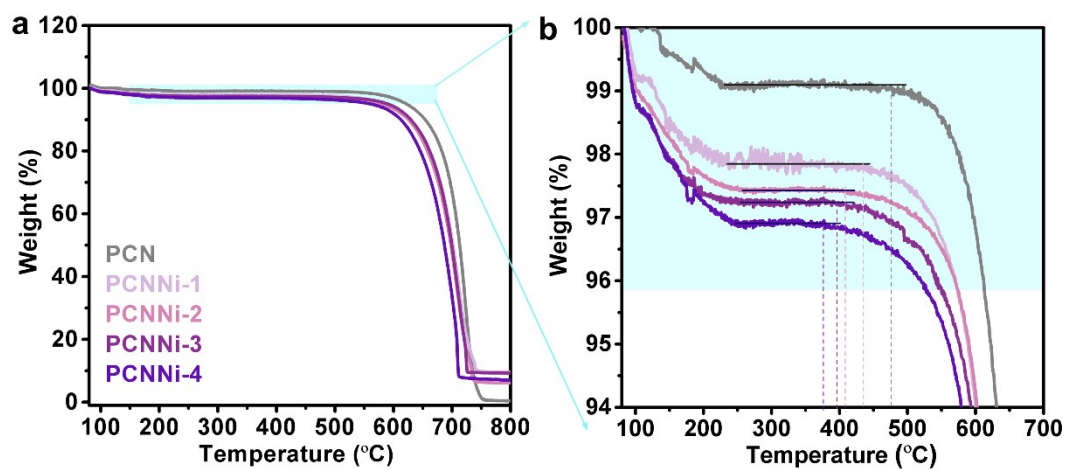

Figure S4. Low-magnification EDX mapping of PCNNi-4

.

Figure S5. Thermogravimetric analysis (TGA) of PCN and PCNNi with different Ni contents.

Nitrogen adsorption and desorption isotherms were provided in Figure S6 in Supporting Information. The Brunauer-Emmett-Teller (BET) specific surface areas (S_{BET}) were calculated to be 5.1, 6.1, 7.3, 7.5 and 8.0 m^2/g for PCN, PCNNi-1, PCNNi-2, PCNNi-3 and PCNNi-4, respectively. This increasing S_{BET} should be due to the small and thin pieces of PCN produced via the polymerization process interrupted by the single-atom Ni. One should also note that S_{BET} does not increase a lot depending on the increasing Ni contents, which should not be responsible to the great improvement in photocatalytic activity.
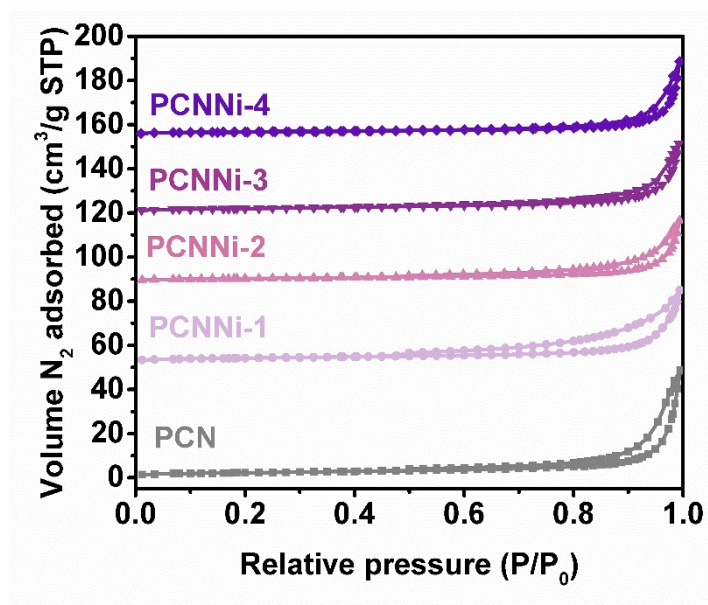

Figure S6. Nitrogen adsorption-desorption isotherms of PCN and PCNNi.

As shown in Figure S7, the Ni 2p peaks of PCNNi-1, PCNNi-2 and PCNNi-4 are observed to locate at 855.0 eV and 872.4 eV, together with two satellite peaks at 860.59 eV and 879.5 eV, indicating the presence of Ni in PCNNi. It was previously recorded that the Ni 2p XPS peaks for $Ni^{\delta+}$ in Ni_3N and Ni^0 in metallic are located at 852.7 eV (870.8 eV) and 853.2 eV (871.3 eV) [14], responsibility. Meanwhile, no peak assigned to Ni-based species is observed in the XRD (Figure 1b). These comparative results of XRD and Ni 2p XPS could confirm that Ni_3N and metal Ni nanoparticle would not form in PCNNi. Two C 1s peaks centered at 284.6 eV and 288.2 eV are attributed to the sp^2 hybridized C-C bonds and sp^2-bonded carbon in the aromatic ring (N=C-N). The peak locating at 286.1 eV means that the sp^2 C atoms are bonded to the amine (-NH_2/-NH-) groups in the aromatic rings [15]. The C 1s XPS spectra of PCNNi are detected unchangeably as compared to that of PCN, indicating the similar chemical environments of C atoms, which are not disturbed by the introduction of single-atom Ni.
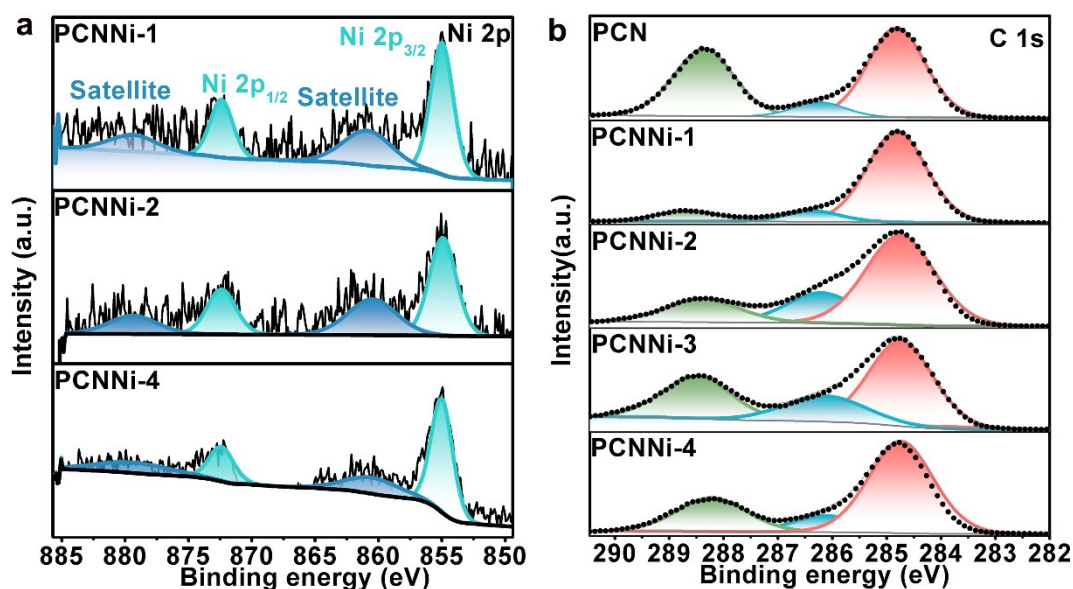

Figure S7. a) Ni 2p XPS analysis of PCNNi-1, PCNNi-2 and PCNNi-4, b) C 1s XPS spectra of PCN and PCNNi with different Ni contents.

As shown in Figure S8a, the NMR spectrum of PCN displays two well-resolved resonances at about 165 and 157 ppm, corresponding to the C(e) atoms in the terminal $CN_2(NH_2)$ or $CN_2(NH)$ of heptazine units and the C(i) atoms in the CN_3 of heptazine units (Figure S8b), respectively. The NMR spectra of PCNNi could be fitted with two peaks analogous to PCN, suggesting the well-preserved heptazine-based structure in PCNNi. According to the detailed assignment of ^{13}C CP-MAS NMR spectra (Figure S8a), both peak C(e) and peak C(i) were located at lower chemical shifts than that of PCN, which indicates that the electron densities of aromatic conjugated rings are reduced [16, 17]. This observation again implies the charge transfer from N atoms (N_A and N_B) to single-atom Ni by Ni-N chemical bonding, which would result in the reduced
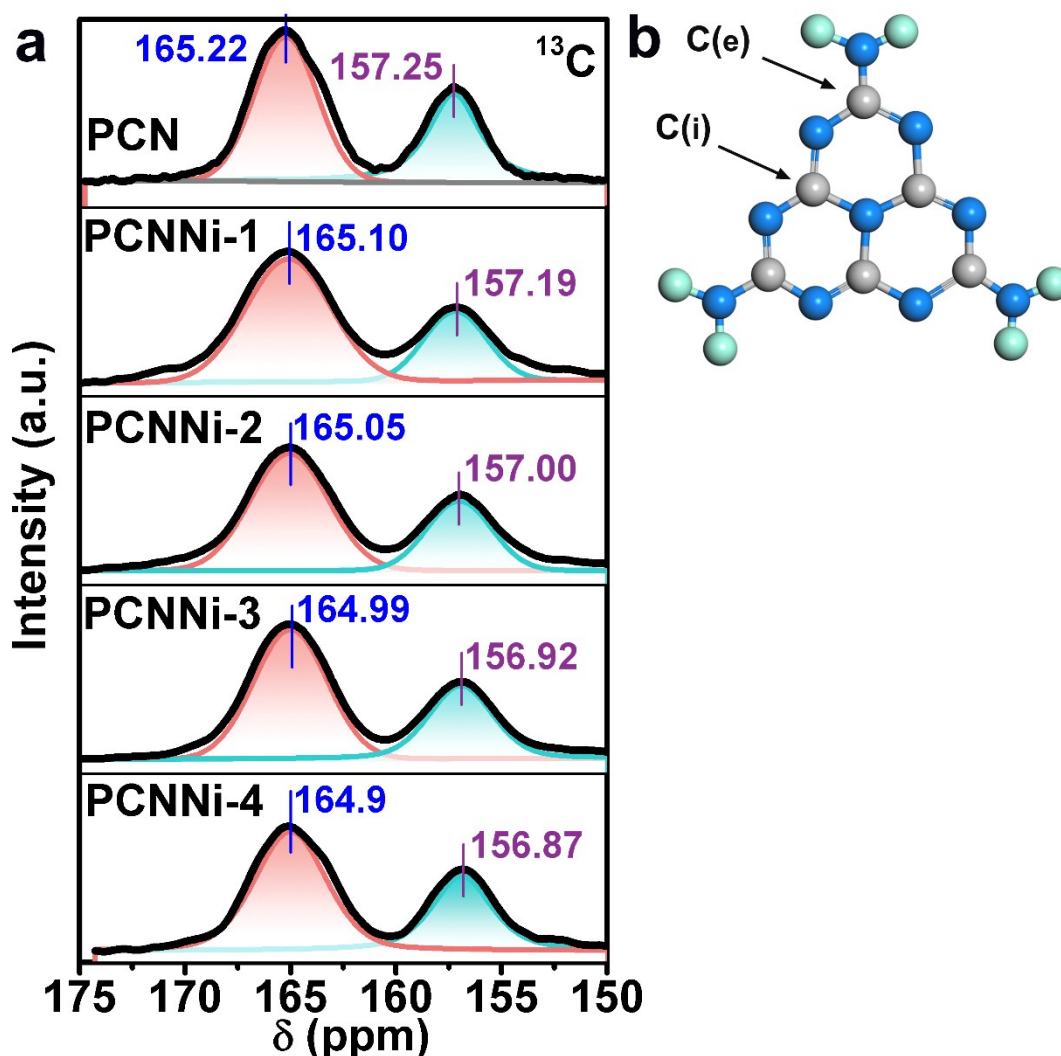
electron densities of aromatic conjugate rings, as previously evidenced by the XPS and XAS analysis.

Figure S8. a) Solid-state ^{13}C CP-MAS NMR spectra of PCN and PCNNi, b) atomic model of molecular structure of heptazine unit.

As shown in Figure S9, the Ni 2p XPS peaks located at 855.0 eV and 872.4 eV suggest that the Ni species in PCNNi-390, PCNNi-425 and PCNNi-500 are nickel ion. No peaks appeared at 853.2 eV indexed to Ni^0, indicating that nickel ion is well isolated in the framework of intermediate products.
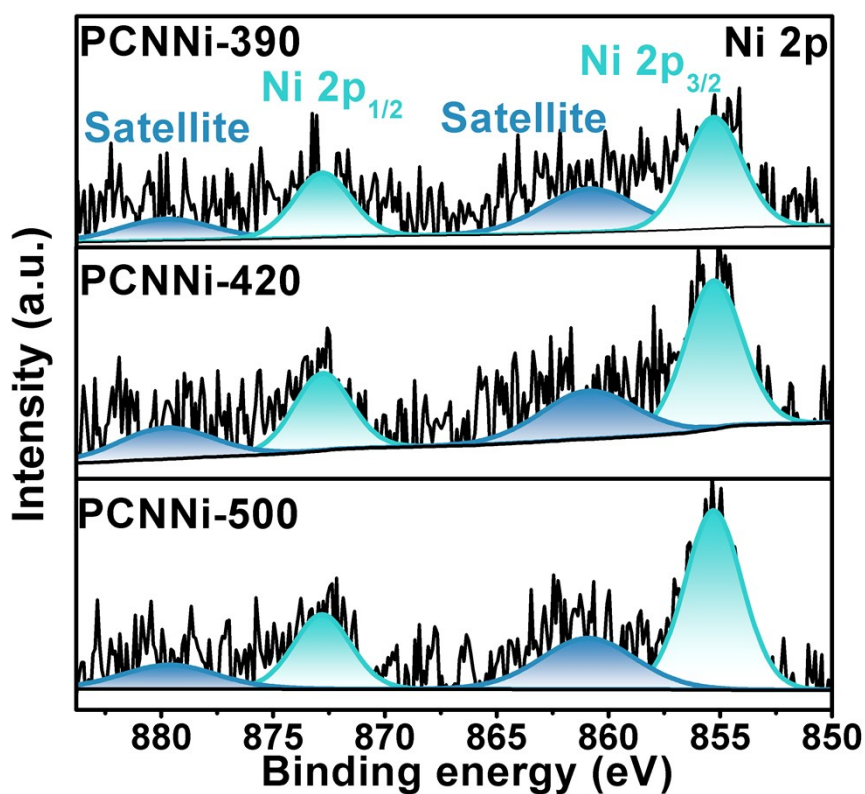

Figure S9. Ni 2p XPS spectra of PCNNi-390, PCNNi-425 and PCNNi-500.

To investigate the terminating effects of single-atom Ni coordinating with N sites during thermal polymerization, special attentions have been focused on the interaction between Ni and coordinated N sites in intermediates obtained at different temperatures during thermal polymerization. Intermediate products such as heptazine ring (390 °C), melem (425 °C) and melon (500 °C) without Ni (named as PCN-390, PCN-425 and PCN-500) and with Ni (named as PCNNi-390, PCNNi-425 and PCNNi-500) were obtained by stopping the reaction at the designed temperatures in closed glass tubes [18]. The intermediate products, heptazine, melem and melon, possess the triangular edge nitrogen (sp^2 N_A), amino groups/ bridge nitrogen (sp^3 N_B) and central tertiary nitrogen (N_C). As shown in Figure S10, both peak N_A and peak N_B are measured to shift to higher binding energies for PCNNi-390, PCNNi-425 and PCNNi-500, as compared to PCN-390, PCN-425 and PCN-500, respectively. This observation indicates that single-atom Ni could coordinate with N sites in heptazine rings formed at the early stage of thermal polymerization. One can also find that the binding energy of peak N_C has no change, confirming that Ni atoms will not coordinate with N_C in the intermediate products or the final PCNNi samples.
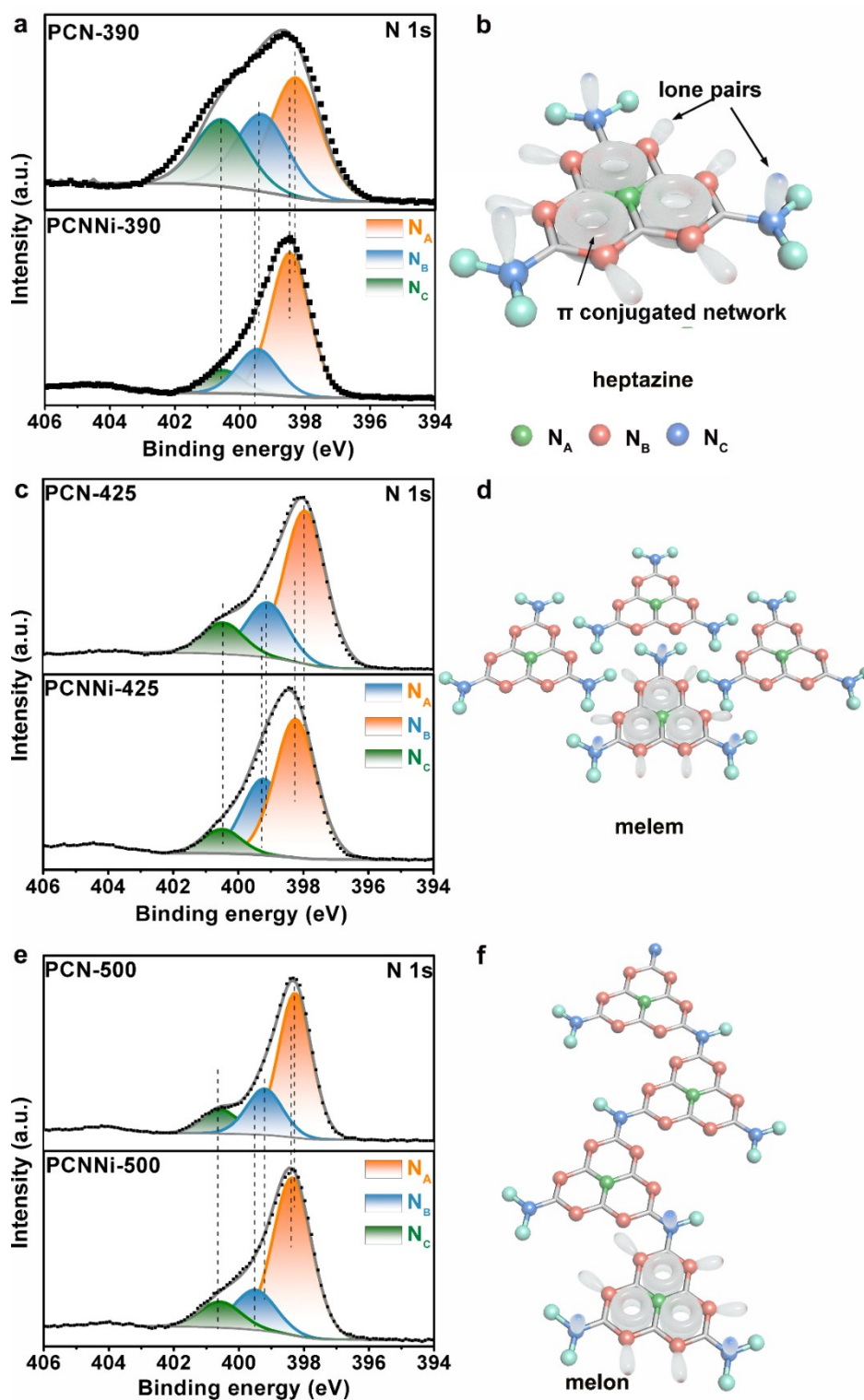
Figure S10. N 1s XPS spectra of a) PCN-390 and PCNNi-390. b) Atomic model of molecular structure for heptazine. c) N 1s XPS spectra of PCN-425 and PCNNi-425. d) Atomic model of molecular structure for melem. e) N 1s XPS spectra of PCN-500 and PCNNi-500. f) Atomic model of molecular structure for melon.
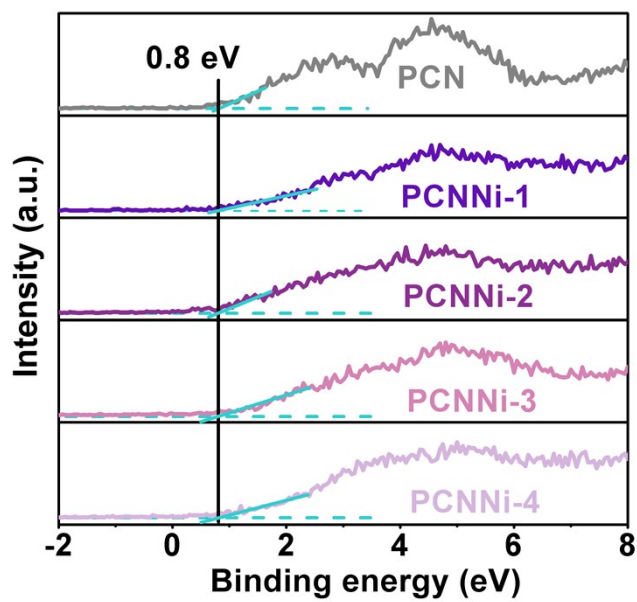
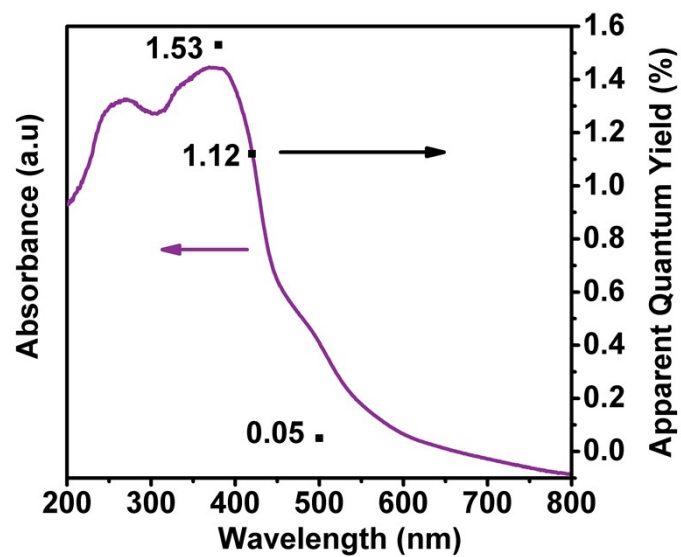Figure S11. XPS valence band spectra of PCN and PCNNi.

Figure S12. The apparent quantum yields of PCNNi-3 for H_2 evolution at 380 nm, 420 nm and 500 nm.

The retention time of H_2 is about 1.1 min and the retention time of O_2 is about 3.5 min. The peak of O_2 was not detected, indicating the oxidative product was not O_2.
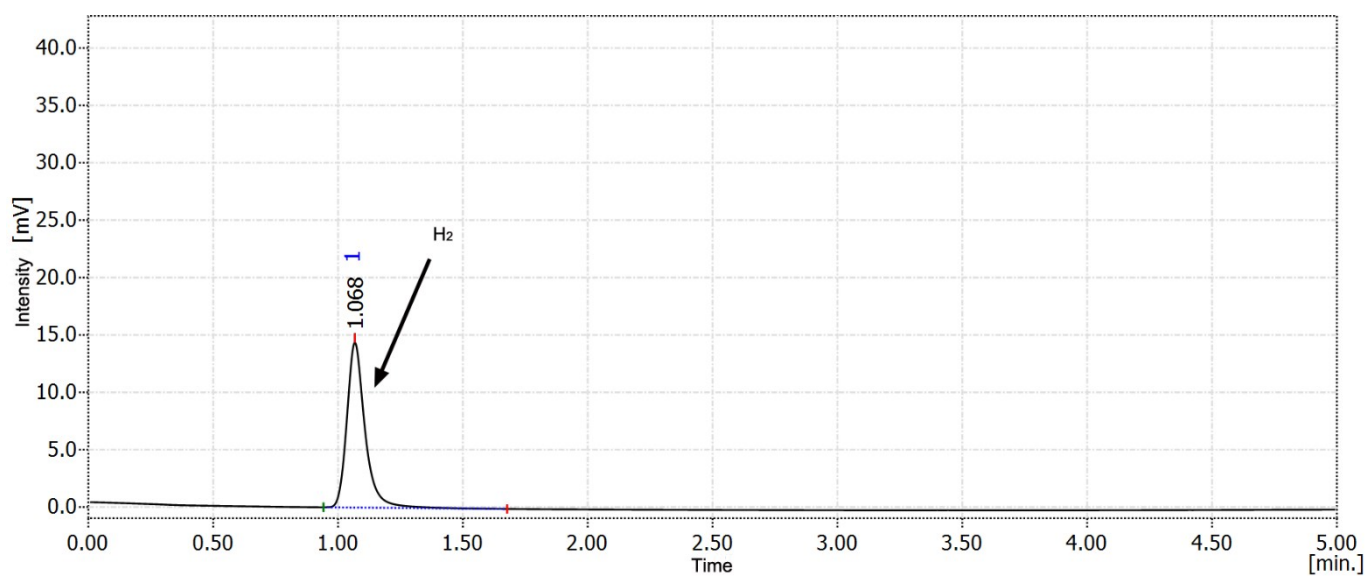

Figure S13. The raw GC spectrum of gas products during photocatalytic overall water splitting over PCNNi detected by using the thermal conductivity detector (TCD).
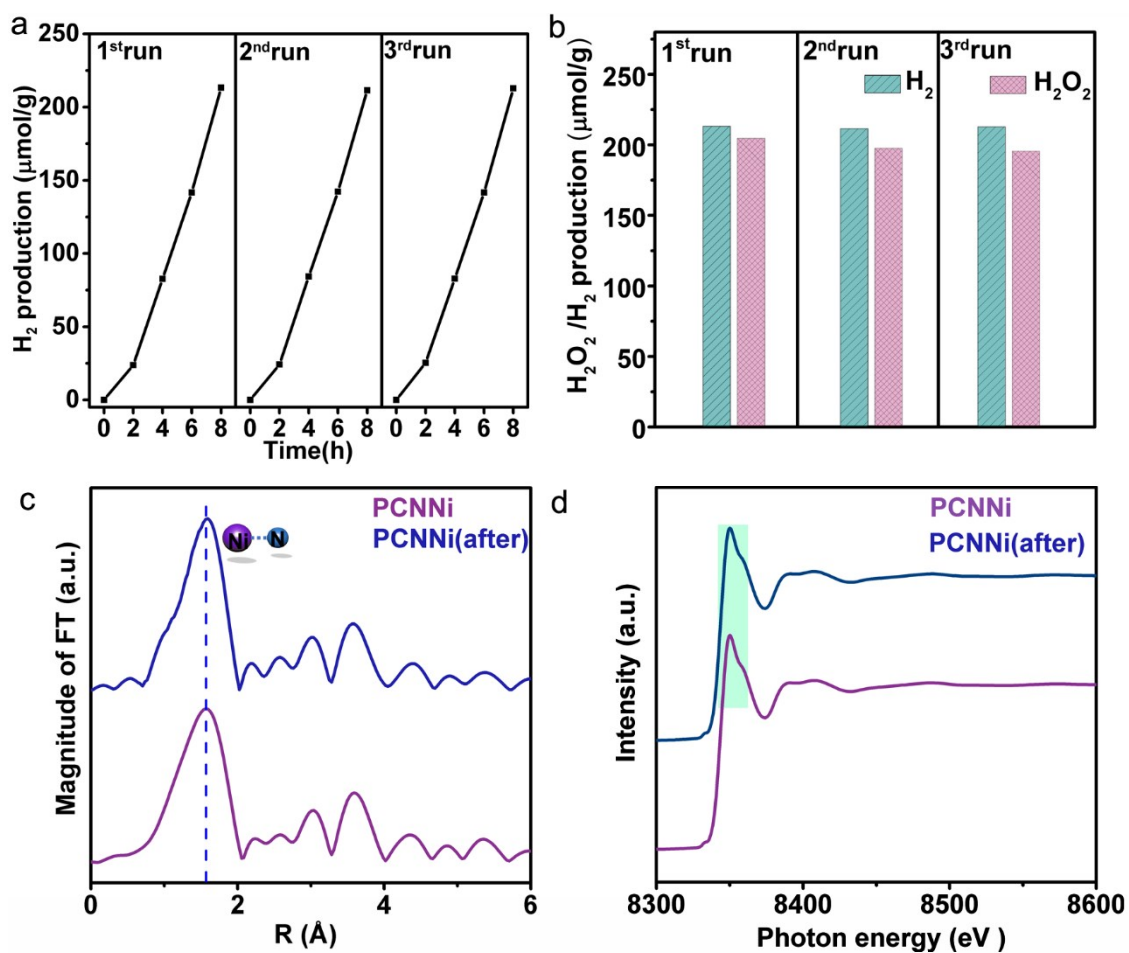
Figure S14. a) Photocatalytic hydrogen generation of PCNNi-3 from pure water under visible light (λ > 420 nm). b) Photocatalytic overall water splitting of PCNNi-3 into hydrogen and hydrogen peroxide without any sacrificial agent under visible light (λ > 420 nm), the reaction system was evacuated after each run cycle. c) Fourier Transformed (FTs) amplitude of extended X-ray absorption fine structure (EXAFS) of Ni K-edge spectra for PCNNi before and after photocatalytic reaction. d) Ni K-edge XANES spectra for PCNNi before and after photocatalytic reaction.
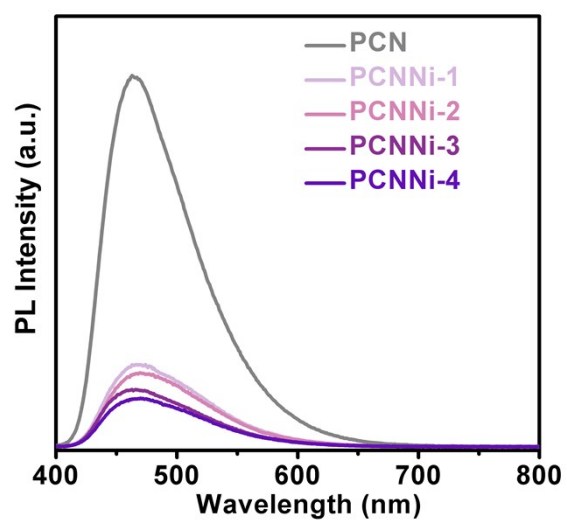
Figure S15. The steady-state PL spectra of PCN and PCNNi.

The electrochemical impedance spectroscopy (EIS) could be used as an effective method to display the charge separation efficiency [19]. In general, a smaller arc radius in the EIS Nyquist plot illustrates the improved charge separation. As shown in Figure S16, PCNNi exhibits decreased charge-transfer resistances (R_{ct}) (1914 Ω for PCNNi-1, 1525 Ω for PCNNi-2, 739 Ω for PCNNi-3, and 1161 Ω for PCNNi-4), compared with PCN (4783 Ω), suggesting that the single-atom Ni terminating agent could greatly improve charge separation. With the increasing Ni contents in PCNNi, the R_{ct} is gradually increased. However, further increase in Ni contents would decrease the R_{ct} of PCNNi-4.
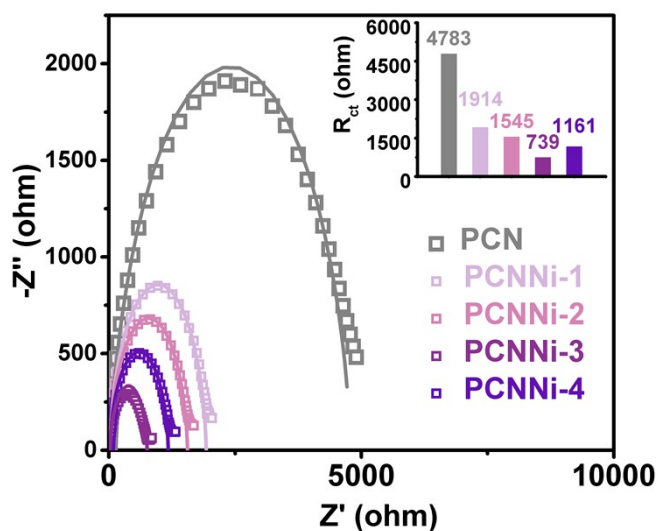
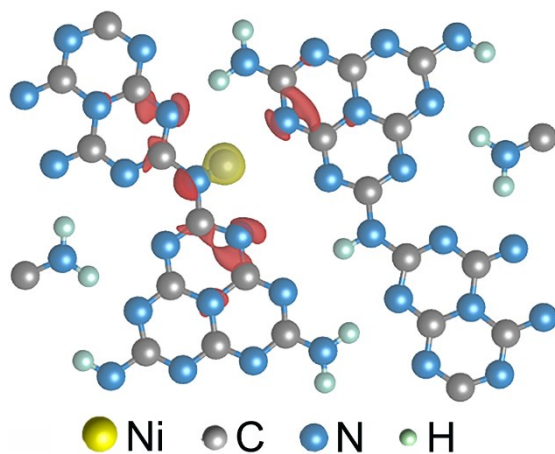Figure S16. Electrochemical impedance spectra of PCN and PCNNi.

Figure S17. Differential charge density mapping of the M-L unit (single-atom Ni coordinated with sp^3 N_B atoms). Red and yellow represents electron accumulation and electron depletion regions, respectively.

As shown in Figure S18a, b, the reaction pathways for water reduction and oxidation for PCNNi with single-atom Ni coordinated with sp^3 N_B were theoretically calculated with free energy diagrams. For water reduction, in comparison to PCN, PCNNi holds a much lower free energy difference of 0.0018 eV for the formation of transition state (TS) for hydrogen evolution (Figure S18a). This can be attributed to the reduced barrier energy of TS formation by the electron accumulation at the reductive active sites of C atoms via MLCT process. For easy understanding, the water reduction reaction pathway is schematically depicted in Figure S18c-f. Single-atom Ni firstly absorbs two H_2O molecules and breaks the H-O-H bond into H and OH (Figure S18c). Then, two H atoms tend to adsorb at the C atom neighboring the single-atom Ni (Figure S18d), and then the H-H bond is formed as the intermediate (Figure S18e), with H_2 releasing from PCNNi finally (Figure S18f). The reaction pathways of water oxidation into H_2O_2 (pathway 1) and O_2 (pathway 2) were also theoretically investigated for PCNNi with single-atom Ni coordinated with sp^3 N_B. As shown in Figure S18b, the free energy difference of 0.4297 eV for TS2.3 is lower that of 0.7738 eV for TS2.4, indicating that HO-OH species rather than O-O species are formed as the intermediates during water oxidation reaction. Meanwhile, the absorption energy of H_2O_2 (0.0724 eV) is lower than that of O_2 (0.1656 eV), resulting in the easier desorption of H_2O_2 from the surface of PCNNi. These results also demonstrate that the oxidation reaction is preferential to generate H_2O_2 rather than O_2 over PCNNi with single-atom Ni coordinated with sp^3 N_B. Figure S18c-f schematically depicted the water oxidation reaction pathway, with the H_2O molecules absorbed at single-atom Ni broken into H and OH (Figure S18c), the two OH adsorb on single-atom Ni (Figure S18d) and then form the TS of HO-OH species (Figure S18e). Subsequently, H_2O_2 is formed and released from the single-atom Ni (Figure S18f).
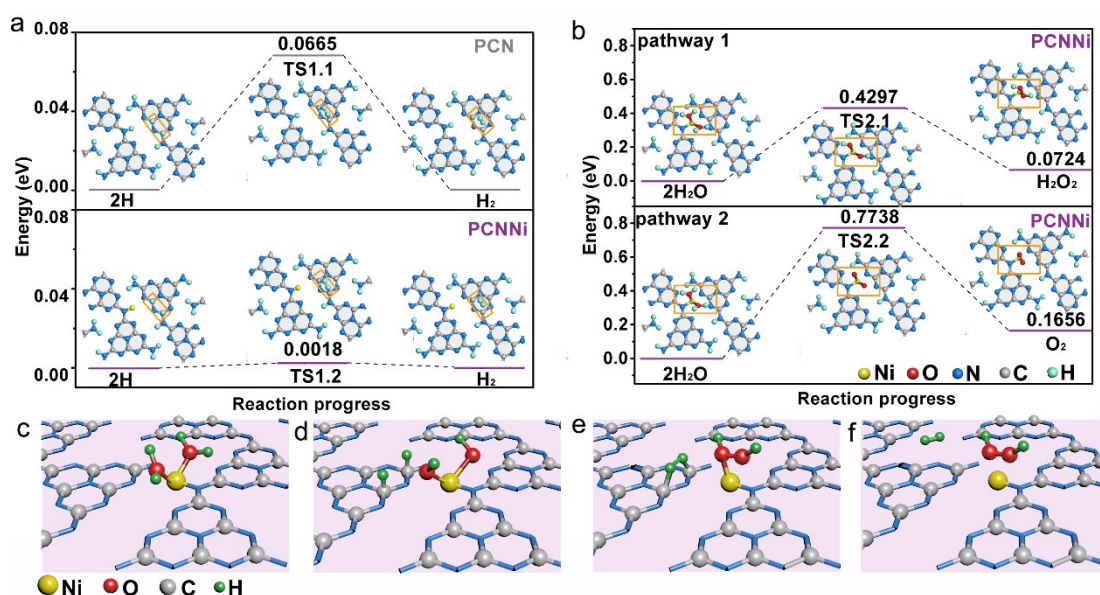

Figure S18. Reaction pathways of a) water reduction into H_2 and b) water oxidation into H_2O_2 (top) and O_2 (down) for PCNNi with single-atom Ni coordinated with sp^3 N_B. c - f) Proposed mechanisms of photocatalytic pure water splitting into H_2 and H_2O_2 for PCNNi with single-atom Ni coordinated with sp^3 N_B.

During the preparation of PCNNi, the melamine and $NiCl_2 \cdot 6H_2O$ were mixed and triturated in agate mortar for 30 min to obtain a well-mixed mixture, and then heated to obtain PCNNi samples. Three batches of PCNNi were synthesized, with Ni contents measured by inductively coupled plasma mass spectrometry (Table S1). The parallel experimental results show that the Ni contents could be well controlled in PCNNi synthesized in different batches.

Table S1. Ni contents of PCNNi synthesized in three batches. The parallel experimental results show that the Ni contents in PCCNi could be controlled in different (I, II and III) synthesis batches.

Sample	Ni content (wt%)			Average value of Ni content (wt%)	Average value of Ni content (wt%) with one decimal place kept
	I	II	III		
PCNNi-1	0.308	0.350	0.314	0.324	0.3
PCNNi-2	0.520	0.566	0.537	0.541	0.5
PCNNi-3	0.921	0.940	0.854	0.905	0.9
PCNNi-4	1.892	1.872	1.924	1.896	1.9

Table S2. FWHM of PCN and PCNNi. FWHM values were calculated by the software of XPSPEAK.

	PCN	PCNNi-1	PCNNi-2	PCNNi-3	PCNNi-4
FWHM	1.86	1.91	1.99	2.21	2.36

Table S3. Elemental analysis results of PCN and PCNNi.

	N content (at%)	C content (at%)	C/N molar ratio	N/C molar ratio
PCN	51.41	34.66	0.674	1.483
PCNNi-1	52.86	34.65	0.6556	1.525
PCNNi-2	47.68	31.12	0.653	1.532
PCNNi-3	51.65	33.01	0.639	1.564
PCNNi-4	52.94	33.49	0.633	1.581

Table S4. Summary of N 1s core-level binding energies of PCN and PCNNi.

	Peak N_A (eV)	Peak N_B (eV)	Peak N_C (eV)
PCN	398.40	399.60	400.90
PCNNi-1	398.49	399.63	400.90
PCNNi-2	398.61	399.69	400.95
PCNNi-3	398.61	399.70	400.95
PCNNi-4	398.73	399.76	400.95

References

1   Y. Li, Z. Wang, T. Xia, H. Ju, K. Zhang, R. Long, Q. Xu, C. Wang, L. Song, J. Zhu, J. Jinag, Y. Xiong, *Adv. Mater.* 2016, **28**, 6959.
2   J. Liu, Y. Liu, N. Liu, Y. Han, X. Zhang, H. Huang, Y. Lifshitz, S. T. Lee, J. Zhong, Z. Kang, *Science* 2015, **347**, 970.
3   G. Kresse, J. Hafner, *J. Phys. Rev. B* 1993, **47**, 558.
4   G. Kresse, J. Furthmüller, Comput. *Mater. Sci.* 1996, **6**, 15.
5   G. Kresse, J. Hafner, *Phys. Rev. B* 1994, **49**, 14251.
6   G. Kresse, D. Joubert, *Phys. Rev. B* 1999, **59**, 1758.
7   J. P. Perdew, K. Burke, M. Ernzerhof, *Phys. Rev. Lett.* 1996, **77**, 3865.
8   W. Tang, E. Sanville, G. Henkelman, *J. Phys.: Condens. Matter* 2009, **21**, 084204.
9   E. Sanville, S. D. Kenny, R. Smith, G. Henkelman, *J. Comp. Chem.* 2007, **28**, 899.
10 G. Henkelman, A. Arnaldsson, H. A. Jónsson, *Comput. Mater. Sci.* 2006, **36**, 354.
11 B. Choudhury, K. K. Paul, D. Sanyal, A. Hazarika, P. K. Giri, *J. Phys. Chem. C* 2018, **122**, 9209.
12 W. J. Ong, L. L. Tan, Y. H. Ng, S. T. Yong, S. P. Chai, *Chem. Rev.* 2016, **116**, 7159.
13 S. Uemura, M. Aono, K. Sakata, T. Komatsu, M. Kunitake, *J. Phys. Chem. C* 2013, **117**, 24815.
14 W. Ni, A. Krammer, C. Hsu, H. Chen, A, Schüler, X. Hu, *Angew. Chem. Int. Ed*. 2019, **58**, 7445.
15 W. Lei, D. Portehault, R. Dimova, M. Antoniettit, *J. Am. Chem. Soc.* 2011, **133**, 7121.
16 B. Zhang, H. Asakura, J. Zhang, J. Zhang, S. De, N. Yan, *Angew. Chem. Int. Ed*. 2016, **55**, 8319.
17 D. Grekov, T. Vancompernolle, M. Taoufik, L. Delevoye, R. M. Gauvin, *Chem. Soc. Rev*. 2018,**47**, 2572.
18 A. Thomas, A. Fischer, F. Goettmann, M. Antonietti, J. O. Müller, R. Schlögl, J. M. Carlsson, *J. Mater. Chem.* 2008, **18**, 4893.
19 M. Wang, C. Dong, Y. Huang, Y. Li, S. Shen, *Small* 2018, **14**, 1801756.